



## High-strength epoxy nanocomposites for 3D printing

Nadim S. Hmeidat, James W. Kemp, Brett G. Compton\*

Mechanical, Aerospace, and Biomedical Engineering Department, University of Tennessee, Knoxville, Knoxville, TN 37996, USA



### ARTICLE INFO

#### Article history:

Received 11 November 2017

Received in revised form

19 February 2018

Accepted 8 March 2018

Available online 9 March 2018

#### Keywords:

3D printing

Epoxy

Composites

Nanoclay

Thermoset

### ABSTRACT

Clay-based nanoscale filler materials are commonly used to impart unique and desirable properties to polymer resins. Small volume fractions of nanoclay have disproportionately large effects on stiffness, toughness, strength, and gas barrier properties of polymer matrices due to their high surface-to-volume ratio and platelet morphology. Recent work has suggested that highly loaded epoxy/clay/fiber mixtures possess desirable rheological properties for use as feedstock materials for direct-write 3D printing, but little is known about the effects of the deposition process on the resulting properties of the printed composites. In this work we characterize the effects of a functionalized nanoclay on the rheological properties and printing behavior of an epoxy resin in the absence of fiber reinforcements, and investigate the effects of clay content and the deposition process on the thermo-mechanical properties of the resulting 3D-printed epoxy/clay nanocomposites. The rheological properties of ink formulations containing up to 12.5 wt% nanoclay are measured using parallel plate rheometry, and the thermo-mechanical properties of the printed composites are measured using 3-pt flexural testing, dynamic mechanical analysis, and thermo-gravimetric analysis. Flexural strength values range from 80 MPa to 100 MPa for cast samples and printed samples tested transverse to the printing direction, and up to 143 MPa for printed samples tested parallel to the print direction. Although the observed anisotropic strength values indicate that the deposition process does impart orientation to the nanoclay, the strength in each direction is significantly greater than values reported for 3D printed thermoplastic composites, suggesting that the epoxy/clay system has high potential for further development as a 3D printing feedstock material.

© 2018 Elsevier Ltd. All rights reserved.

### 1. Introduction

Nano-scale layered silicates (nanoclays) show great promise as filler materials to improve the strength, stiffness, toughness, gas barrier, and flame retardant properties of polymer resins [1–5]. The exceptional property enhancements are mainly attributed to the high surface-to-volume ratio and platelet morphology of nanoclays, which results in high interfacial area and interaction volume between the filler and matrix, and enables the platelets to be oriented through certain processing routes like solvent casting [6], and high shear extrusion [7]. The nanoclay/epoxy system, in particular, has received considerable attention because of the desirable mechanical, thermal, and chemical properties of cross-linked epoxy resins, and the favorable interaction chemistry between the epoxy pre-polymer and the nanoclay materials [1,4,5,8–11]. However, the high surface area of the nanoclay platelets leads to large increases

in viscosity when added to epoxy resins [9], which can present challenges during processing using traditional methods such as casting or infiltration. Recently, Compton and Lewis demonstrated that nanoclays can be used in epoxy/short fiber composite inks for direct-write (DW) additive manufacturing (AM) to impart nearly ideal rheological properties (a high degree of shear thinning, and yield stress behavior) for extrusion-based 3D printing [12]. Since this work, there has been significant effort in 3D printing of polymer matrix composites in general [13–16], and rapid progress in 3D printing of epoxy-based composite materials containing silica, clays, fibers, and functional materials [17–22], specifically. These works have demonstrated significant improvements in elastic modulus (up to 57 GPa in tension) [22] and control of filler orientation and architecture [17,23] compared to earlier work [12,24,25], but basic 3D-printable epoxy/nanoclay systems have not been thoroughly characterized and investigated in the context of AM. In this work we investigate effects of nanoclay content on the rheology, printing behavior, and thermomechanical properties of an epoxy-based DW feedstock in the absence of fibers or functional

\* Corresponding author.

E-mail address: [bcompto1@utk.edu](mailto:bcompto1@utk.edu) (B.G. Compton).

filler materials.

AM is the process of building components in an incremental, additive fashion through either direct material deposition or selective material consolidation within a vat or powder bed. Traditional polymer AM technologies use either thermoplastic feedstocks that are liquefied in a heated deposition nozzle prior to deposition, as is the case with fused deposition modeling (FDM), fused filament fabrication (FFF), and big area additive manufacturing (BAAM), or are selectively sintered in a powder bed using a laser (selective laser sintering – SLS), or they utilize liquid polymer precursors that cross-link when exposed to ultraviolet light during or directly after deposition, as is the case for stereolithography (SLA) and polymer jetting. DW 3D printing is somewhat different in that viscoelastic feedstocks are deposited via extrusion through fine nozzles at room temperature without requiring melting prior to, or curing immediately after, deposition. In this process, shown schematically in Fig. 1a, the feedstocks must possess sufficient yield stress and shear thinning behavior that they can be readily extruded through fine nozzles, but quickly recover high viscosity and elastic behavior in order to maintain shape after deposition [26,27]. Because the process proceeds at ambient temperature, it has the potential to alleviate the geometric warping and residual stresses that arise in 3D printed thermoplastic materials due to the strong thermal gradients that result from the heating and cooling associated with deposition [28–31]. It is important to note that thermosets do experience shrinkage during curing [32] that can lead to warping in geometrically complex parts. However, shrinkage can be limited through the choice of curing agent and filler material, and preliminary experiments on large-scale AM of thermoset polymers show significant promise [33]. Additionally, with thermoset materials printed using DW, curing occurs well after deposition, so that chemical crosslinks form between printed layers, potentially leading to drastic improvements in bond strength between layers compared to printed thermoplastics, which are plagued with low strength in the build direction [34–36].

Here, we report the effects of alkyl quaternary ammonium-functionalized nanoclays on the rheological, printing, thermal, and mechanical properties epoxy/clay nanocomposites fabricated

via DW 3D-printing. In our approach, the nanoclay is used as both the viscosifying agent to impart beneficial rheological properties that enable DW printing, and as mechanical reinforcement in the cured composite. Inks are formulated containing fixed amounts of epoxy resin and nanoclay platelets up to 12.5 wt%. The rheological properties of each ink formulation are experimentally investigated using parallel plate rheometry, and the thermo-mechanical properties of the printed composites are measured using 3-pt flexural testing, thermo-gravimetric analysis (TGA), and dynamic mechanical analysis (DMA). The effect of deposition on the orientation of clay platelets and associated anisotropic strength and stiffness is probed by testing specimens parallel (hereafter referred to as *longitudinal* specimens) and transverse (hereafter referred to as *transverse* specimens) to the printing direction. Cast and printed behavior is compared for one ink formulation, and a control ink formulated using isotropic fumed silica is also investigated for comparison. Good printing behavior is observed in inks with shear yield stress values greater than ~300 Pa, and observed strength values are up to ~5x higher than those reported in Ref. [12] for epoxy/clay DW inks without fibers, suggesting there is great potential for further development of this material system for additive manufacturing.

## 2. Experimental

### 2.1. Materials

The epoxy resin used in this study is Epon 826 epoxy resin (Momentive Specialty Chemicals, Inc. Columbus, OH), a Bisphenol A diglycidyl ether (DGEBPA) resin with 178–186 wt per epoxide, and density of 1.162 g/cc. 1-Ethyl-3-methylimidazolium dicyanamide (EMIM DCA) was used as a latent curing agent (Basionics VS03, Sigma-Aldrich, Inc. St. Louis, MO). This imidazole-based curing agent results in inks with up to one month of shelf stability at room temperature and also imparts a characteristic reddish-brown to black color to the cured composite [37]. Garamite 7305 nanoclay (BYK-Chemie GmbH, Wesel, Germany) with a specific density of 1.5–1.7 g/cc was utilized as the nano-scale filler material. Garamite 7305 is part of BYK's patented Mixed Mineral Thixotrope

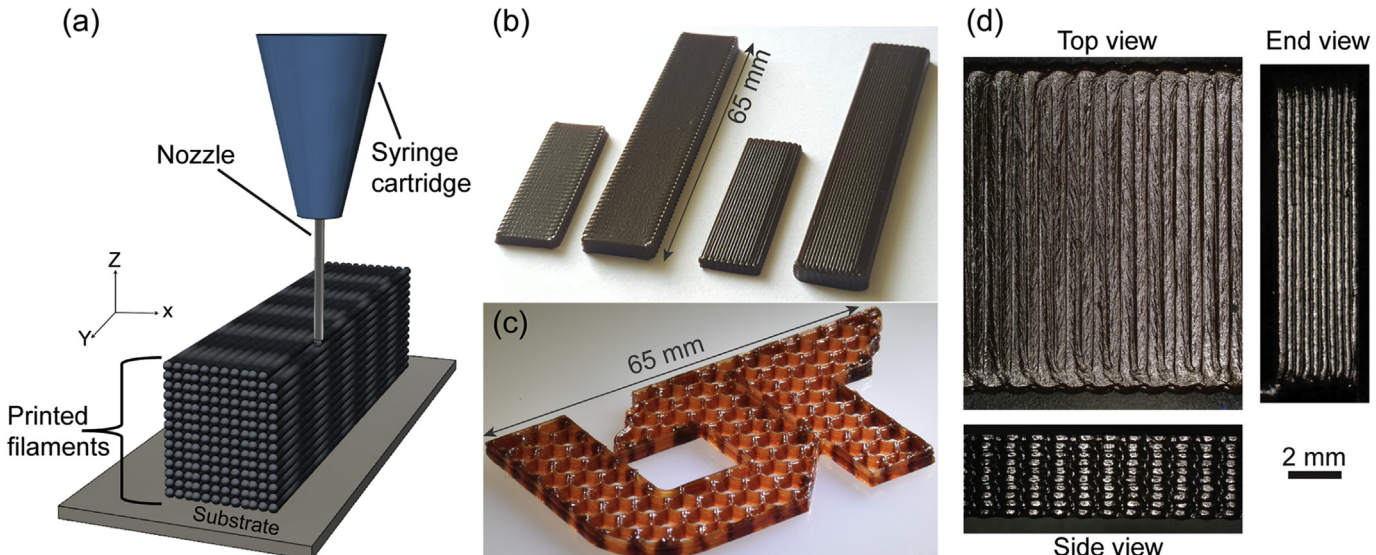


**Fig. 1.** (a) Schematic illustration of direct write 3D-printing. (b) 3D-printed rectangular specimens for both flexural and DMA test characterization, with transverse specimens on the left and longitudinal specimens on the right. (c) 3D-printed University of Tennessee logo with honeycomb infill. (d) Top, side, and end view optical micrographs of a transverse flexure specimen printed using the 12.5 wt% nanoclay ink formulation.

technology and is comprised of a blend of benzalkonium sepiolite and benzalkonium montmorillonite [38,39], alkyl quaternary ammonium-modified silicates with fibrous and layered crystal structures, respectively [1,5,40,41]. As described in the following sections, this nanoclay blend readily disperses in epoxy and other polar polymer resins and imparts strong rheology modification at fairly low loading. Additionally, one ink formulation was made using fumed silica (Cab-o-sil TS-720, Cabot Corporation, Alpharetta, GA) instead of nanoclay as a control ink for comparison. Fumed silica is often used as a viscosifier in epoxy resins, and has been previously demonstrated to yield 3D-printable epoxy inks [24,25,42]. Fumed silica particles, however, do not possess strong anisotropy, so they would not be expected to adopt any preferred orientation during the printing process. Comparisons between nanoclay- and fumed silica-based inks may thus provide greater insight into the specific effects of the printing process and filler type on the mechanical properties of 3D-printed composites.

## 2.2. Formulation

The inks were prepared by mixing the epoxy resin with appropriate amounts of nanoclay (or fumed silica), using a centrifugal planetary SpeedMixer (FlackTek, Inc. Landrum, SC) in 185-mL plastic containers. Six formulations, plus the control, were prepared using 30 g of Epon 826 resin and 1.5 g of the curing agent (VS03). The contents were mixed under vacuum at 0.1 atm for 60 s at 1700 rpm. Next, the nanofiller was added, followed by 60 s of mixing at 1700 rpm and 0.1 atm. After mixing with the nanofiller, the sides of the container were scraped with a spatula and mixed for an additional 60 s at 1800 rpm and 0.1 atm to make sure that the nanoclay was completely dispersed and the mixture was bubble free. The compositions of all epoxy/clay ink formulations are summarized in Table 1.

## 2.3. 3D printing

Ink formulations containing 7.5, 10 and 12.5 wt% nanoclay and 10 wt% fumed silica were printed using a custom DW 3D-printing platform comprised of a 3-axis positioning stage (Shopbot Tools, Inc. Durham, NC), solenoid valves, and a voltage controlled air pressure regulator (Omega Engineering, Inc. Norwalk, CT). Inks were manually loaded into 10 cc syringe barrels (Nordson EFD, Westlake, OH) using a spatula. To eliminate bubbles, all loaded syringe barrels were centrifuged at 4500 rpm for 10 min using a Sorvall<sup>TM</sup> ST-8 Centrifuge (ThermoFisher Scientific, Waltham, MA). The RPM and duration were chosen empirically to effectively remove bubbles without causing any separation of the clay from the epoxy resin, following [12]. Following the centrifuging process, the loaded syringe was inserted into a pressure adapter (HP3, Nordson EFD, Westlake, OH). A 634-micron-diameter straight metal Luer-lock syringe tip (McMaster-Carr, Elmhurst, IL) was used

to print all samples. Layer height was specified as 0.6 times the nozzle diameter (380.4 µm). Longitudinal and transverse test specimens were printed using translation speeds of 30 mm/s and 20 mm/s, respectively. Ink formulations with 0, 2.5 and 5 wt% clay were too fluid to 3D print and were instead cast into printed silicone molds of the same dimensions as the printed samples. To provide a comparison between cast and printed specimens of the same formulation, additional specimens were made using the formulation containing 5 wt% clay by 3D-printing it into a silicone mold. In this manner, any orientation of the clay that results from the printing process should be preserved, and may manifest in the mechanical properties or microstructural observations. All inks were printed or cast onto glass substrates covered with PTFE-coated aluminum foil (Bytac, Saint-Gobain Performance Plastics, Worcester, MA) to prevent a permanent bond to the substrate. All samples were pre-cured at 100 °C for 24 h, allowed to cool down at room temperature, removed from the substrate, and finally cured at 220 °C for 2 h on an uncoated glass substrate. The g-code defining the print path for all test samples was generated using custom programs written with Scilab software (Scilab Enterprises, France). Representative 3D-printed DMA and flexure samples are shown in Fig. 1b. The print path for the UT logo shown in Fig. 1c was generated from a computer-aided design (CAD) solid model that was converted to an.stl file and sliced for FFF printing using the open source slicing software, Slic3r (<http://slic3r.org/>). The software-generated tool path was then converted for use on our direct-write printer using a custom conversion program.

## 2.4. Characterization

Rheological properties of the inks were measured using a Discovery HR-2 Rheometer (TA Instruments, New Castle, DE) with a gap size of 500 µm for all inks. All measurements were preceded by a 2 min conditioning step at a constant shear rate of 0.1/s. Oscillatory stress sweeps were performed at controlled oscillatory stresses from (5–5000 Pa) and continuous flow sweeps were performed at controlled shear rates from (0.02–100 1/s). Tests were conducted at ambient lab temperature (~21 °C).

TGA was carried out on a Q500 by TA instruments. The tests were run to 800 °C at a ramp rate of 10 °C/min under both air and nitrogen atmospheres. Samples were cut from cured printed or cast bars using a low speed sectioning saw (TechCut 4, Allied High Tech Products, Inc. Rancho Dominguez, CA). DMA was performed on a Discovery HR-2 Rheometer using three-point bending configuration at a constant oscillation frequency of 1 Hz. DMA test specimens had nominal dimensions of 32 × 12 × 2 mm, and testing was conducted over a temperature range of 25–250 °C at a heating rate of 3 °C/min. Three-point flexural tests were conducted at room temperature on an electromechanical load frame (Model 45, MTS Systems Corporation, Eden Prairie, MN, USA) using a 1 kN or 5 kN load cell (typical loads were 200–300 N and no systematic difference was observed between measurements from the 1 kN and 5 kN load cells). Flexural test samples had target as-printed dimensions of 65 × 12.7 × 3.2 mm, and were tested using a span length of 50 mm and cross-head speed of 1.3 mm/min. Edges and surfaces of the flexural tests samples were ground or machined smooth prior to testing, so that the final as-tested depth of the majority of samples fell between 2.95 mm and 3.15 mm, resulting in a span-to-depth ratio of between 16.95:1 and 15.87:1, which is very close to the 16:1 span-to-depth ratio specified in ASTM D790 [43]. Optical micrographs were recorded using a VHX-5000 digital microscope (Keyence Corporation of America, Itasca, IL). Density was measured using the Archimedes method.

**Table 1**  
Compositions of epoxy/nanoclay formulations.

Ink #	Resin (g)	VS 03 (g)	Clay (g)	Clay (wt.%)	Clay (calculated vol%)	Density (g/cc)
1	30	1.5	0.00	0.0	0.0	1.190
2	30	1.5	0.81	2.5	1.871	1.206
3	30	1.5	1.66	5	3.77	1.214
4	30	1.5	2.55	7.5	5.69	1.220
5	30	1.5	3.50	10	7.63	1.230
6	30	1.5	4.50	12.5	9.60	1.250

### 3. Results and discussion

#### 3.1. Rheology

Curves of the apparent viscosity as a function of shear rate are plotted in Fig. 2a for each ink formulation investigated. The neat epoxy resin exhibits nearly rate-independent viscosity at  $\sim 10$  Pa s for the range of shear rates probed. The addition of nanoclay drastically increases the apparent viscosity and shear thinning behavior of the epoxy resin. At low shear rates ( $10^{-2}$  s $^{-1}$ ), the apparent viscosity increases to 3000 Pa s for 2.5 wt% nanoclay, and up to  $4 \times 10^5$  Pa s for 12.5 wt% nanoclay. At shear rates comparable to those experienced by the material during deposition ( $\sim 50$  s $^{-1}$ ) the apparent viscosity values range from 10 to 100 Pa s, a much smaller range indicative of the high degree of shear thinning imparted by the nanoclay. The shear thinning behavior of complex fluids can be quantified by fitting the apparent viscosity vs shear rate curves to a power law of the form

$$\eta = K\dot{\gamma}^{n-1} \quad (1)$$

where  $K$  is the consistency index and  $n$  is the flow index. The flow index,  $n$ , describes the rate dependence of the fluid; for shear thinning fluids,  $n < 1$ , while for shear thickening fluids,  $n > 1$ , and for Newtonian fluids,  $n = 1$ . On a log-log plot of apparent viscosity vs shear rate, as in Fig. 2a, the slope of the linear portion of the apparent viscosity curve is equal to  $1-n$ . Numerical values for  $n$  and

$K$  were computed from the rheology curves by linear regression over the linear portions of the curves (i.e. between 1 and 100 s $^{-1}$  for the neat resin, and between 0.01 and 1 s $^{-1}$  for all other formulations). The computed  $n$  and  $K$  values are plotted in Fig. 2b for all formulations. It can be seen that the consistency index correlates strongly with the amount of clay, while presence of any nanoclay results in a flow index much less than one, without a strong correlation between amount of nanoclay and flow index. All formulations containing greater than 2.5 wt% clay exhibit flow index values less than 0.1, indicating superior shear thinning behavior. It is worth noting that the precise value of the flow index is very sensitive to the exact range of the apparent viscosity curves used in the linear regression. For consistency, we have used the same range for all curves containing clay, but small adjustments to the range change the computed values of flow index slightly. Dedicated studies will be needed to investigate the relationships between

**Table 2**  
Rheological properties of epoxy/nanoclay formulations.

Clay (wt.%)	$G'_0$ (kPa)	$\tau_y$ (Pa)	$K$ (Pa.s $^n$ )	$n$
0.0	—	—	6.24	0.995
2.5	0.1183	24.8	58.6	0.1130
3.5	1.622	58.9	163.6	0.0885
5	18.69	122.9	369	0.00324
7.5	63.0	343	1329	0.0276
10	176.3	822	3160	0.0399
12.5	273	1050	4790	0.0479

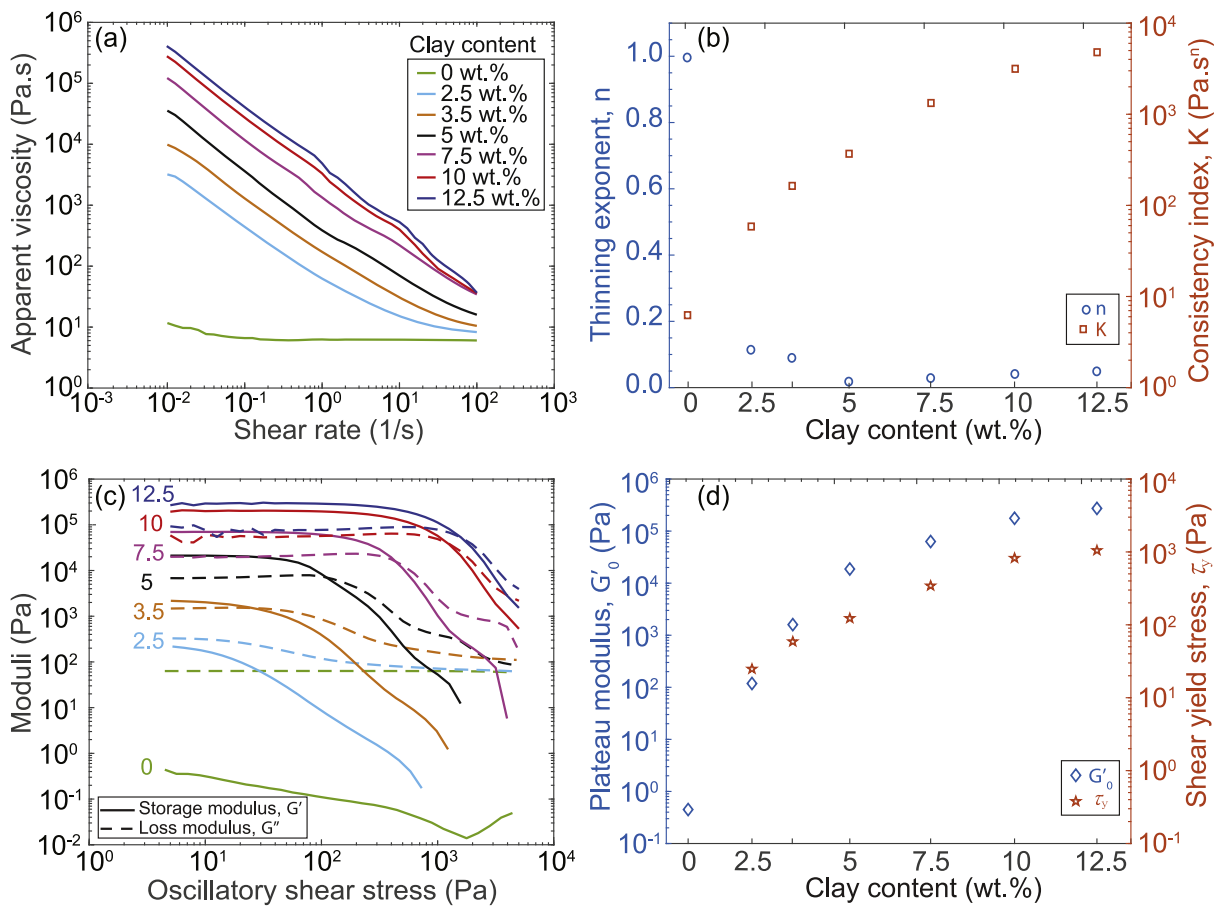


**Fig. 2.** Rheological behavior of all epoxy/nanoclay formulations investigated. (a) Log-log plots of apparent viscosity as a function of shear rate. (b) The shear thinning exponent,  $n$ , and the consistency index,  $K$ , computed by fitting the linear portions of the viscosity curves in (a) with the power-law fluid model described by equation (1). (c) Log-log plots of storage and loss moduli as a function of oscillatory shear stress. (d) The plateau elastic modulus and the shear yield stress values for each formulation, measured from (c).

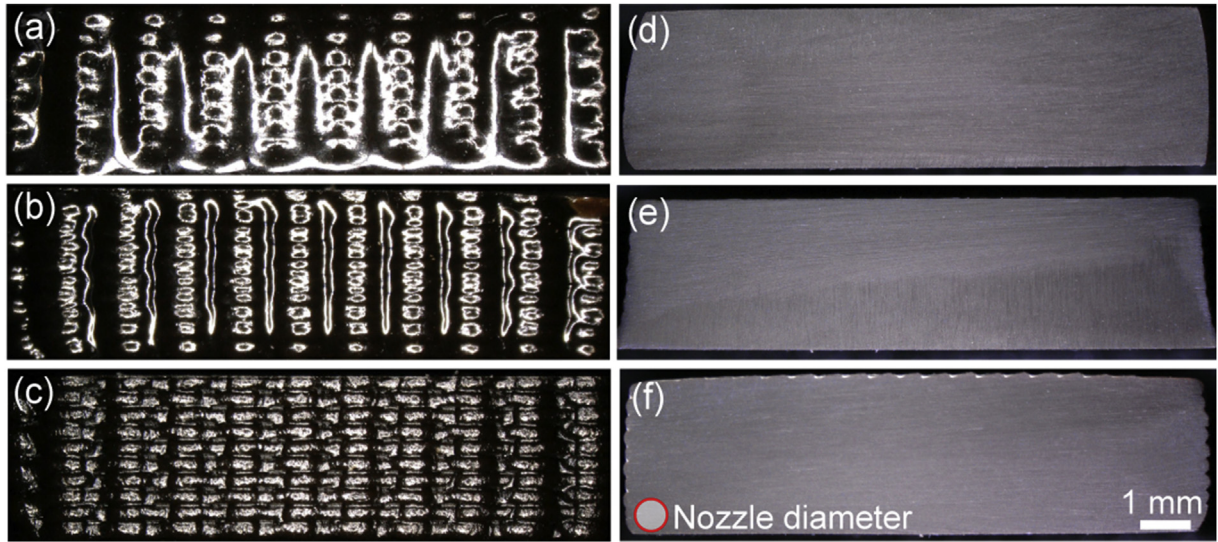


**Fig. 3.** Optical micrographs of the as-printed ends of representative longitudinal flexural bars along with corresponding optical micrographs of cross-sections of the same bars. (a) and (d) contain 7.5 wt% nanoclay, (b) and (e) contain 10 wt% nanoclay, and (c) and (f) contain 12.5 wt% nanoclay. These micrographs demonstrate that all formulations can form fully dense components without any voids trapped between filaments.

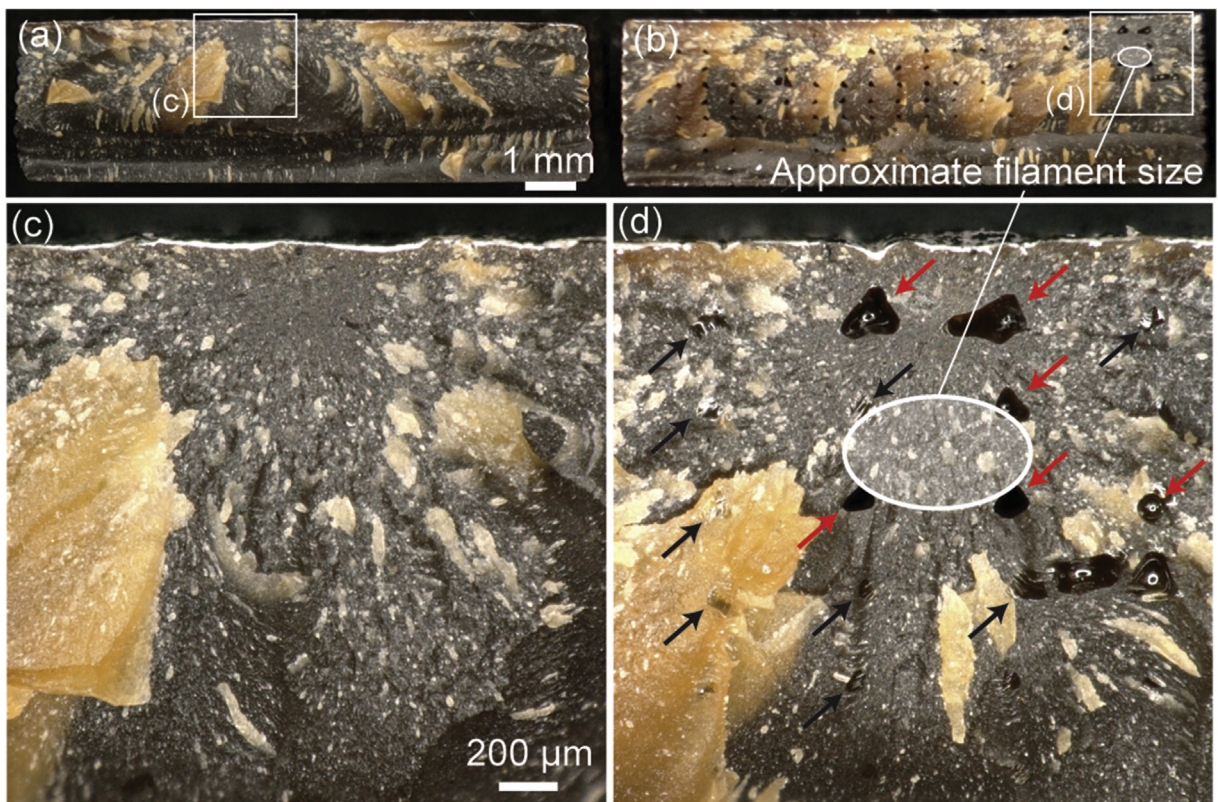


**Fig. 4.** Optical micrographs showing printing-related voids in a longitudinal flexure specimen containing 12.5 wt% clay. (a) Low-mag image of the fracture surface of a pore-free sample. (b) Low-mag image of the fracture surface of a sample containing a regular array of interfilamentary voids resulting from a lower ink flow rate during printing. (c) High-mag micrograph of the pore-free surface shown in (a). (d) High-mag micrograph of the surface containing voids shown in (b). The approximate filament size is indicated by the white oval. Empty pores are indicated with red arrows, while filled pores are indicated with black arrows. (For interpretation of the references to color in this figure legend, the reader is referred to the Web version of this article.)

potential variations in the degree of exfoliation of the clay in these systems and subtle changes in the flow and consistency indices. For the purposes of this study, all formulations containing clay exhibit favorable shear thinning.

Plots of the storage ( $G'$ ) and loss moduli ( $G''$ ) are shown on Fig. 2c. The neat resin displays a stress-independent loss modulus value of ~100 Pa that is approximately three orders of magnitude larger than the storage modulus, indicating that the neat resin

behaves predominantly as a viscous fluid. The addition of nanoclay increases both the loss and storage moduli. At higher clay content (>2.5 wt%) the storage modulus exceeds the loss modulus, and the inks begin to display solid-like behavior at low shear stress. In this case, the storage modulus remains constant over a certain range. This constant value is known as the *plateau elastic modulus*,  $G'_0$ , and for the formulations characterized, the values range from  $1.87 \times 10^3$  Pa, for the formulation containing 3.5 wt% clay, up to  $2.7 \times 10^5$  Pa for the formulation containing 12.5 wt% clay. For those formulations possessing solid-like behavior, as the applied stress increases above a certain value, the storage modulus decreases precipitously to a value below that of the loss modulus, and more liquid-like behavior is obtained. This transition corresponds to the *shear yield stress*,  $\tau_y$ , which can be measured from the intersection point of two tangent lines drawn from the stress-independent elastic region of the storage modulus curve and the shear thinning portion of the storage modulus curve [44]. Shear yield stress values increase with increasing clay content from 59 Pa for the 3.5 wt% formulation to  $1.05 \times 10^3$  Pa for the 12.5 wt% formulation. The values of plateau elastic moduli and the shear yield stress for each formulation are plotted in Fig. 2d and all measured rheological parameters are summarized in Table 2.

### 3.2. 3D printing and sample fabrication

Through a series of printing tests, it was observed that inks containing 5 wt% clay and less, did not possess sufficiently solid-like behavior to print multiple layers without significant flow and spreading of the lower layers, so flexural specimens were cast, rather than printed. The ink formulations containing greater than 5 wt% clay were able to be extruded through the deposition nozzle reliably at and above 120 psi (827 kPa), and recovered sufficiently solid-like behavior after deposition to enable flexural test specimens comprising ten layers to be printed with minimal spreading or other geometric distortion. Because of the rheological requirements of 3D printing, the printable formulations were not able to be cast for comparison. Instead, the 5 wt% clay formulation was printed into silicone molds in the longitudinal and transverse motifs to provide a direct comparison between casting and 3D printing using the same ink.

Optical micrographs of the ends of representative longitudinal flexure specimens are shown in Fig. 3 along with corresponding cross-sections of the same bars. In each of the views, the axis of the printed filaments is normal to the plane of the image, so that the surfaces shown in Fig. 3a–c are where the print head makes a U-turn, as shown in Fig. 1d. For the ink containing 7.5 wt% nanoclay (Fig. 3a), the surface of the printed part is smooth and shiny. The locations of individual printed filaments are still visible as smooth peaks or undulations in the surface, but most of the definition is lost because the filaments have flowed together during deposition. As clay content and shear yield stress increase, the individual filaments in each layer become more defined on the exterior surface of the printed bars. On the specimen printed using the 10 wt% nanoclay ink (Fig. 3b), the printed layers have mostly coalesced, but the repeated identical print path for each layer results in columnar features on the surface that indicate the print paths. For the sample printed using the 12.5 wt% nanoclay formulation (Fig. 3c), the surface features are sharp and all layers and filaments are visible. Cross-sections of printed flexural bars (Fig. 3d–f) show that, despite the stark difference in surface appearance (and rheological properties) between the inks with different nanoclay content, fully dense, pore-free components can be successfully printed with a wide range of ink compositions, provided flow rate, layer height, and print speed are chosen appropriately. As an example of printing-related voids that can occur if printing parameters are not

carefully tuned, fracture surfaces of two specimens printed using the 12.5 wt% clay formulation are shown in Fig. 4. The fracture surface shown in Fig. 4a and c is the result of carefully tuned print parameters for this ink and nozzle combination. No voids are visible, nor is any evidence of the print path. The surface shown in Fig. 4b and d contains a regular array of round voids with a characteristic spacing equal to the nozzle diameter, very similar to those observed in thermoplastic 3D printing. This sample was printed with a flow rate that was slightly too low for the print speed.

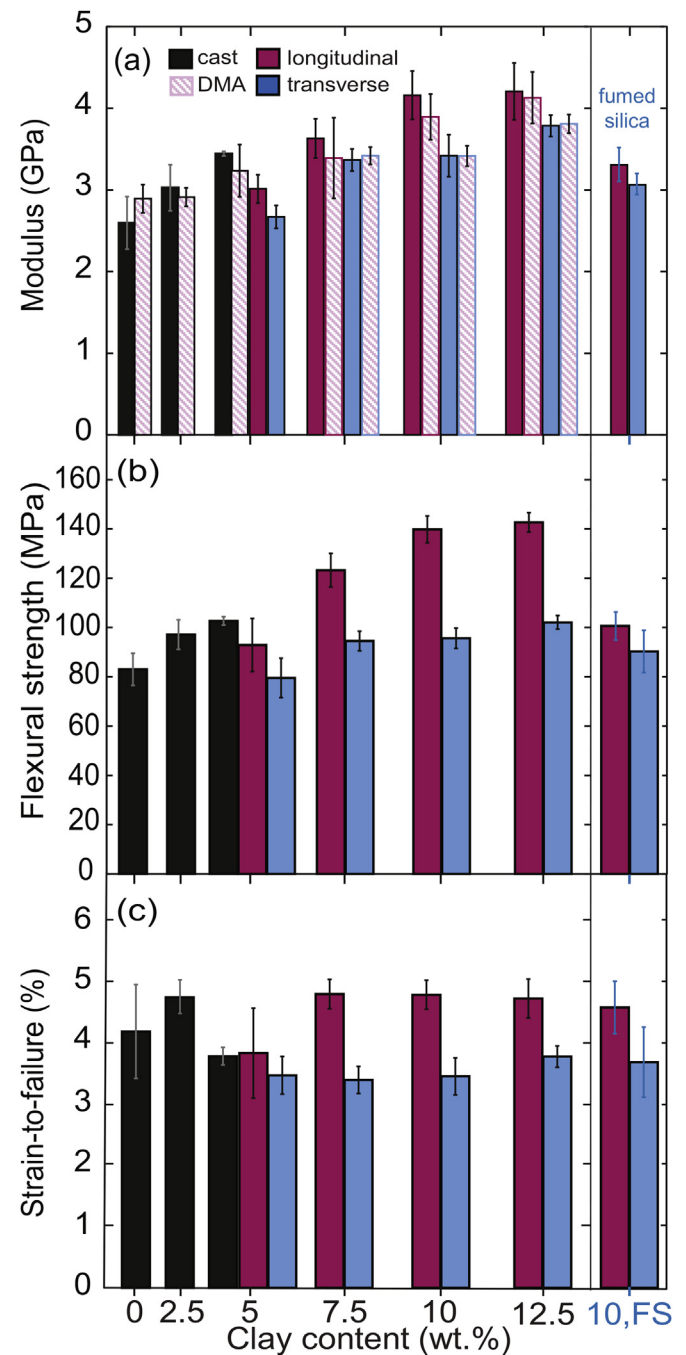


**Fig. 5.** Bar plots of the average values of (a) flexural modulus, (b) flexural strength and (c) strain-to-failure for all tested specimens. The room temperature storage modulus values measured by DMA are also shown in (a) for comparison. The flexural properties of the epoxy/fumed silica printed specimens are also shown on the right side of the bar plots, indicated by FS. Error bars indicate the standard deviation in measured values.

Interestingly, some of the voids in Fig. 4d can be seen to have been filled in with what appears to be neat epoxy resin (indicated with black arrows). It is possible that neat resin may have flowed from the surrounding material as a result of surface tension during the curing process. These observations raise the possibility that thermosets may be able to be designed to be more robust against printing-related voids than thermoplastics. However, it is impossible to make any definitive statements based only on these preliminary observations, and further work would be needed.

### 3.3. Mechanical behavior

The elastic modulus, strength, and strain-to-failure for all cast and printed flexural specimens are plotted in Fig. 5 and summarized in Table 3. Flexural modulus values increase monotonically with increasing clay content from 2.6 GPa for the cast neat epoxy up to 4.2 GPa and 3.8 GPa for the longitudinal and transverse samples containing 12.5 wt% nanoclay, respectively (Fig. 5a). Flexural strength values (Fig. 5b) for all samples tested range from 80 MPa to 143 MPa, with a monotonic increase in strength with clay content for the cast and printed specimens. Among the printed specimens, longitudinal samples exhibited considerably higher strength and

stiffness, suggesting that the printing process imposes a preferred orientation on the clay that leads to anisotropic properties in printed parts. Interestingly, the fumed silica ink exhibits substantially less anisotropy in both strength and stiffness than the clay-containing formulations, although a small amount of anisotropy does remain. This suggests that a small portion of the anisotropy observed in the mechanical tests may be attributed to the printing process alone, while the majority appears to depend on the aspect ratio of the filler material. The fact that the printed 5 wt% formulation exhibited anisotropy and lower strength than the cast 5 wt% formulation would seem to corroborate this interpretation.

Strain-to-failure for all flexural tests ranged from 3% to 5% (Fig. 5c). Longitudinal specimens failed at higher strains than transverse specimens for all printed specimens, including the fumed silica. This may indicate that strength-limiting flaws are more likely to occur between filaments where they would more strongly affect the strength and strain-to-failure of the transverse specimens.

Representative fracture surfaces of the flexural specimens are shown in Fig. 6. In all specimens, the mirror, mist, and hackle regions are apparent and indicate that failure initiated near center of the tensile surface (the top edge in the images). The fracture surface

**Table 3**  
Mechanical properties of cast and 3D-printed epoxy nanocomposites.

Specimen configuration	Clay (wt.%)	Flexural modulus (GPa)	Storage modulus (GPa) <sup>b</sup>	Flexural strength (MPa)	Strain-to-failure (%)	Number of specimens
Cast	0	2.60 ± 0.32	2.89 ± 0.17	83.0 ± 6.51	4.17 ± 0.77	5
	2.5	3.03 ± 0.28	2.91 ± 0.11	97.1 ± 5.99	4.73 ± 0.30	3
	5	3.45 ± 0.03	3.24 ± 0.32	102.7 ± 1.74	3.77 ± 0.14	3
Longitudinal	5	3.01 ± 0.17	--	92.9 ± 10.82	3.82 ± 0.73	6
	7.5	3.62 ± 0.24	3.50 ± 0.41	123.3 ± 6.83	4.78 ± 0.25	9
	10	4.16 ± 0.30	3.90 ± 0.28	140.3 ± 5.50	4.77 ± 0.24	10
	10, FS <sup>a</sup>	3.31 ± 0.21	--	100.6 ± 5.69	4.56 ± 0.43	9
	12.5	4.21 ± 0.35	4.13 ± 0.32	142.7 ± 3.95	4.70 ± 0.30	8
Transverse	5	2.67 ± 0.14	--	79.5 ± 8.00	3.46 ± 0.31	6
	7.5	3.37 ± 0.14	3.42 ± 0.11	94.5 ± 3.97	3.38 ± 0.22	10
	10	3.42 ± 0.26	3.42 ± 0.13	95.6 ± 4.17	3.44 ± 0.30	8
	10, FS <sup>a</sup>	3.06 ± 0.13	--	90.3 ± 8.56	3.67 ± 0.57	9
	12.5	3.79 ± 0.13	3.81 ± 0.12	102.1 ± 2.76	3.76 ± 0.17	8

<sup>a</sup> Fumed silica.

<sup>b</sup> Measured by DMA.

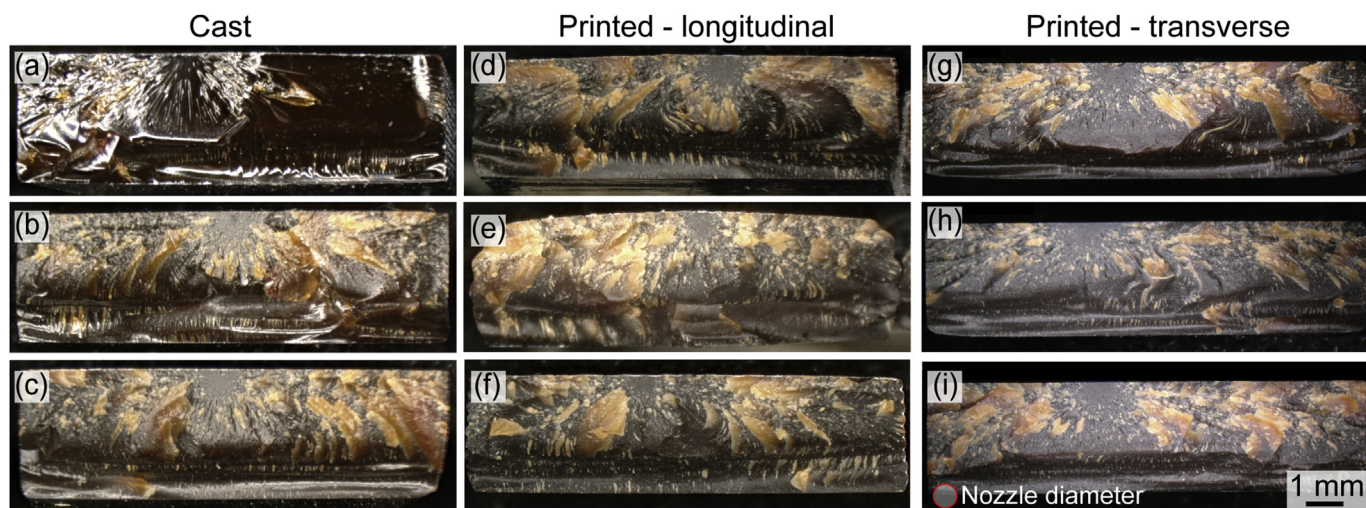


**Fig. 6.** Optical micrographs of representative fracture surfaces of cast and printed flexure specimens containing (a) 0 wt%, (b) 2.5 wt%, (c) 5 wt%, (d) and (g) 7.5 wt%, (e) and (h) 10 wt %, and (f) and (i) 12.5 wt% nanoclay. No inter-filamentary voids are observed, indicating complete coalescence of printed filaments.

of the cast neat epoxy (Fig. 6a) has a smooth glassy appearance typical of brittle unfilled epoxies, while the presence of nanoclay leads to rougher fracture surfaces (Fig. 6b–i) with a higher number of flakes (the light tan regions in the micrographs) that indicate crack bifurcation and higher energy consumption during fracture. The fracture surfaces for the longitudinal and transverse printed specimens (Fig. 6d–i) can be compared in the center and right columns, respectively. There is no evidence of the original print path, pores between printed filaments, or any delamination between layers, suggesting strong bonding between printed filaments and thorough crosslinking between layers. Representative high magnification scanning electron micrographs of the failure initiation points are shown in Fig. 7 for the 10 wt% clay specimens, as well as the fumed silica specimens. The point of failure initiation is visible in each micrograph as a light gray or white particle. These features do not appear to be pores, but may be dust or agglomerates of clay or fumed silica. Interestingly, the features in the transverse specimens (Fig. 7b and d) are considerably larger than those in the longitudinal specimens (Fig. 7a and c). This may be a contributing factor to the decreased strength associated with the transverse specimens.

#### 3.4. Thermal behavior

Thermograms and primary derivative plots are shown in Fig. 8 for all formulations investigated, and data points for the initial degradation temperature (defined as the temperature at 5% mass

loss, following Gu et al. [45]), the temperature at maximum degradation rate, and the char yield at 800 °C are summarized in Table 4. The presence of nanoclay mildly accelerates the onset of thermal degradation and slightly reduces the temperature at which the maximum degradation rate is reached in both nitrogen and air atmospheres. However, beyond the presence or absence of clay, the clay content does not strongly correlate with either measurement. The initial degradation temperature and the temperature at maximum degradation rate are not substantially different in nitrogen or air atmospheres, although the progression of thermal degradation clearly is. In air, mass loss slows substantially between 450 °C and 500 °C and accelerates again between 500 °C and 600 °C (Fig. 8a and b), while in nitrogen, degradation occurs in one step with a significantly higher char yield at 800 °C for all formulations (Fig. 8c and d). The two-step degradation process in air is attributed to the competing formation and oxidation of intermediate carbonaceous products [5,45–47], although Gu et al. point out that the exact mechanisms of this process are not fully understood [45]. The temperature at which the second peak mass loss rate occurs in air (Fig. 8a) increases with clay content, from 529 °C for neat epoxy, up to 569 °C for the formulation containing 12.5 wt% clay. These results are in good agreement with those reported by Camino et al. for similar epoxy/clay systems using an anhydride curing agent [47]. This shift in the second peak mass loss temperature with clay content is attributed to the excellent oxygen barrier properties of clays, which slows the rate of oxidation of the char material [45,47].

Storage modulus and loss tangent curves measured by DMA in

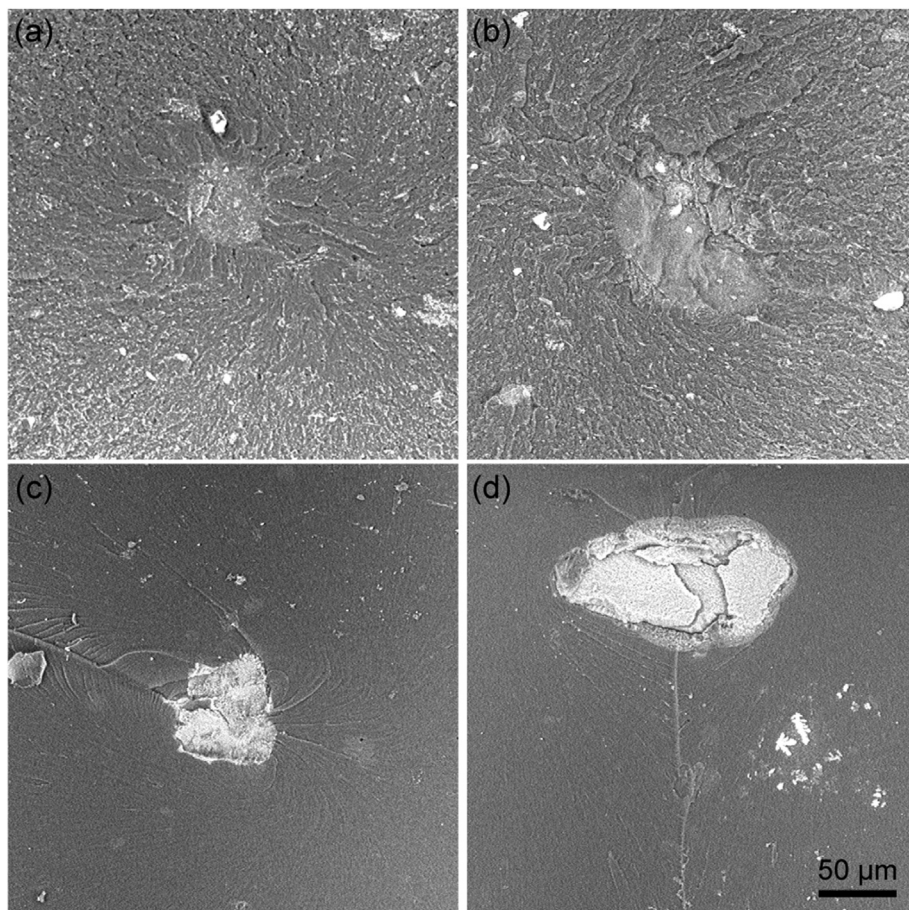


**Fig. 7.** Scanning electron micrographs showing features of the point of failure initiation on the fracture surfaces of (a) a longitudinal specimen containing 10 wt% clay, (b) a transverse specimen containing 10 wt% clay, (c) a longitudinal specimen containing 10 wt% fumed silica, and (d) a transverse specimen containing 10 wt% fumed silica.

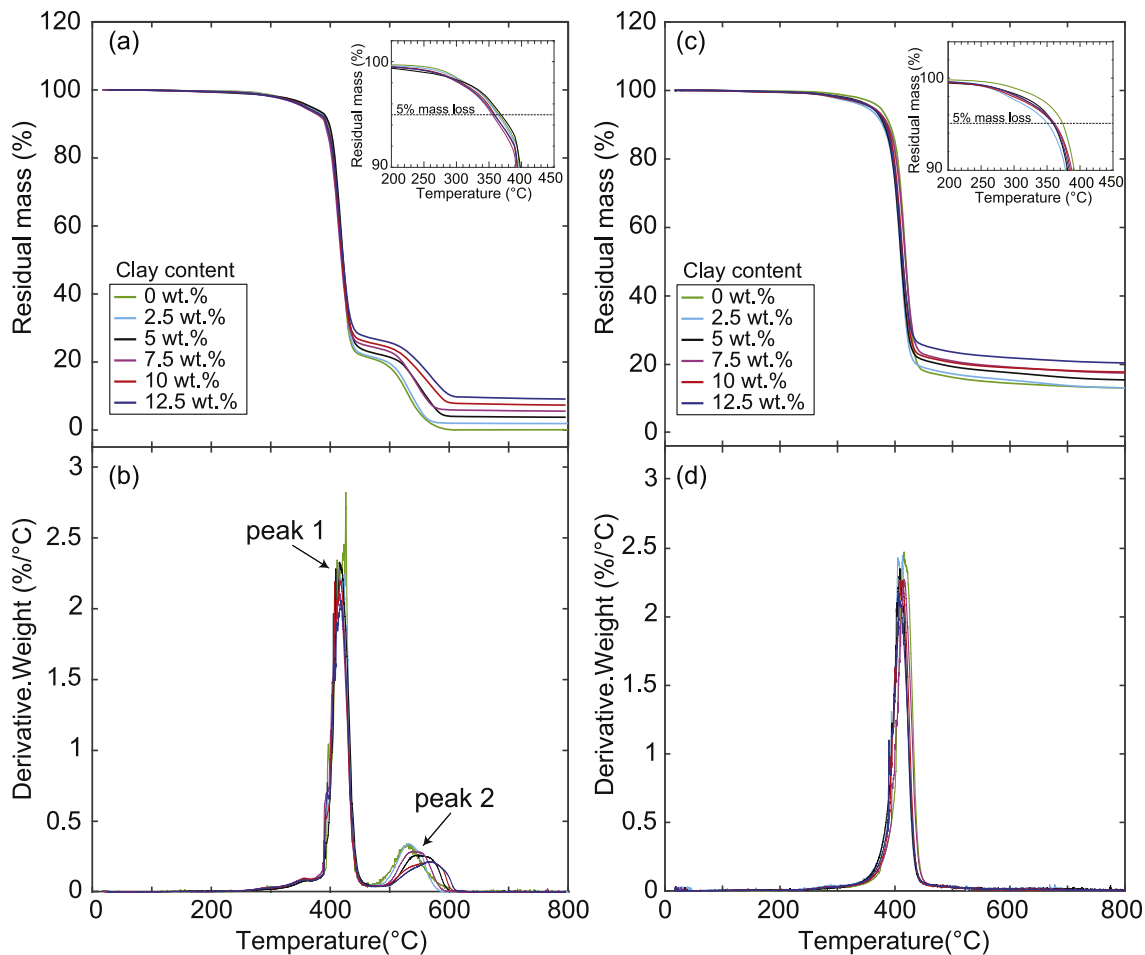


**Fig. 8.** Thermograms and primary derivative plots for the epoxy/clay formulations in (a) and (b) air, and (c) and (d) nitrogen atmospheres.

**Table 4**

Thermogravimetric data for epoxy/nanoclay composites in air and nitrogen atmospheres.

Clay (wt.%)	Air			Nitrogen			
	5% mass loss (°C)	Peak loss rate (°C)		Char yield @800 °C (%)	5% mass loss (°C)	Peak loss rate (°C)	
		Peak 1	Peak 2				
0	365.1	426.2	528.7	0.074	374.2	416.0	13.2
2.5	362.8	419.1	534.6	1.90	351.1	412.9	13.2
5	368.1	415.8	547.9	3.76	360.1	408.8	15.5
7.5	354.8	416.6	539.3	5.55	362.0	415.8	17.5
10	358.8	417.8	569.6	7.33	359.9	413.1	17.8
12.5	357.5	417.9	568.8	9.11	359.4	406.8	20.5

3-pt flexure for each of the formulations investigated are plotted in Fig. 9, and the glass transition temperatures,  $T_g$ , measured using the peak of the loss tangent curve, are plotted in Fig. 10. Storage modulus values at room temperature for each formulation are also plotted in Fig. 5a with the modulus values measured during the quasistatic flexure testing. Elastic modulus measurements are broadly consistent between the two test methods. Peak loss tangent values range from 0.25 to 0.35 and  $T_g$  values range from 149 °C for the neat epoxy to 161 °C for the 7.5 wt% clay formulation. For printed samples, the  $T_g$  measured for transverse samples is 2–5 °C lower than that for the longitudinal samples, indicating a potential effect of the printing process on the arrangement and orientation of the clay platelets.

### 3.5. Anisotropy due to printing

Although the nanoclay particles that are employed here to impart both desirable rheological properties for printing and mechanical reinforcement after curing are significantly smaller than the deposition nozzle, much greater anisotropy in stiffness and strength in printed composites was observed when utilizing these high-aspect-ratio filler materials compared to fumed silica, which has a more isotropic morphology. These observations indicate that the shear flow within the deposition nozzle may impose orientation on the clay platelets that leads to mechanical properties that differ parallel to the printed filament axis and transverse to it. Indeed, anisotropic mechanical properties associated with orientation of nanoclay platelets resulting from shear flow has been

observed in previous studies [7]. However, the fracture surfaces of printed longitudinal and transverse flexural specimens are not significantly different from those of the cast specimens, and no evidence of the original print path can be seen on the fracture surfaces or inferred from the mode of fracture.

In order to investigate the possible architecture imposed on the clay platelets by the printing process, thin slices of material were cut from all cast and all longitudinal printed flexure specimens, including the control samples utilizing fumed silica. These slices were polished, and observed using transmitted light microscopy, with and without crossed polarizers. Micrographs of the thin sections are shown in Fig. 11. In simple transmitted light mode (left-hand column), the interior of all samples appear nearly uniform with a darker perimeter that may be due to oxidation during curing, and a darker central region that may be due to elevated temperature resulting from the exothermic crosslinking reaction. The printed samples (Fig. 11d–h) have characteristic surface pattern from the printing process, but otherwise there are few features to distinguish printed from cast samples. In cross-polarized light mode (right-hand column), however, the effects of nanoclay and the printing process are stark. The crossed polarizers completely extinguish all light passing through the neat cast sample (Fig. 11a), except for small regions at the corners of the sample where some residual stresses may be present, indicating an absence of birefringence throughout the bulk of the sample. The cast samples containing 2.5 wt% and 5 wt% nanoclay (Fig. 11b and c) exhibit a small amount of birefringence in a nebulous pattern throughout the cross-section, and the amount of birefringence increases with clay content, suggesting that it is the presence of the nanoclay that is causing birefringence. In contrast to the cast samples, the entire cross-sections of the printed clay samples (Fig. 11d–g) are visible in cross-polarized light, indicating strong birefringence and orientation of the nanoclay. In fact, a periodic array of higher and lower transmittance is apparent over the entire cross-section, and the size of the repeat units corresponds closely to the size of the nozzle used to print the sample. Images of the cast and printed 5 wt% clay formulation (Fig. 11c and d) allow direct comparison between the casting and printing process and highlight the effects of the high shear flow and discrete deposition process associated with direct-write 3D printing. Interestingly, the printed fumed silica sample exhibits minimal birefringence (Fig. 11h), comparable to the unfilled cast epoxy. These observations provide clear evidence that the printing process imposes order on the clay in the nanocomposite feedstock, rather than the resin itself, and suggests that new studies are needed to more fully understand these effects and how they might be utilized to make better materials or take special advantage of the printing process.

#### 4. Summary and conclusions

In this work, we have investigated the effects of an alkyl quaternary ammonium-functionalized nanoclay blend on the rheology of an epoxy resin as it pertains to formulating printable nanocomposite feedstocks for direct-write 3D printing. We have also characterized relationships between nanoclay content and the printing behavior, and between nanoclay content and the thermo-mechanical properties of printed nanocomposites using 3-pt flexural testing, DMA, TGA, and cross-polarized light microscopy. The strength of these 3D-printed epoxy nanocomposites ranged from 80 to 143 MPa, substantially higher than that of any previously reported values for 3D-printed thermoset composites, including short fiber-reinforced materials. We anticipate higher strength values when fibers are incorporated into the matrix formulations presented here. Although anisotropy in strength and stiffness was observed in the printed nanocomposites, the layer-to-layer

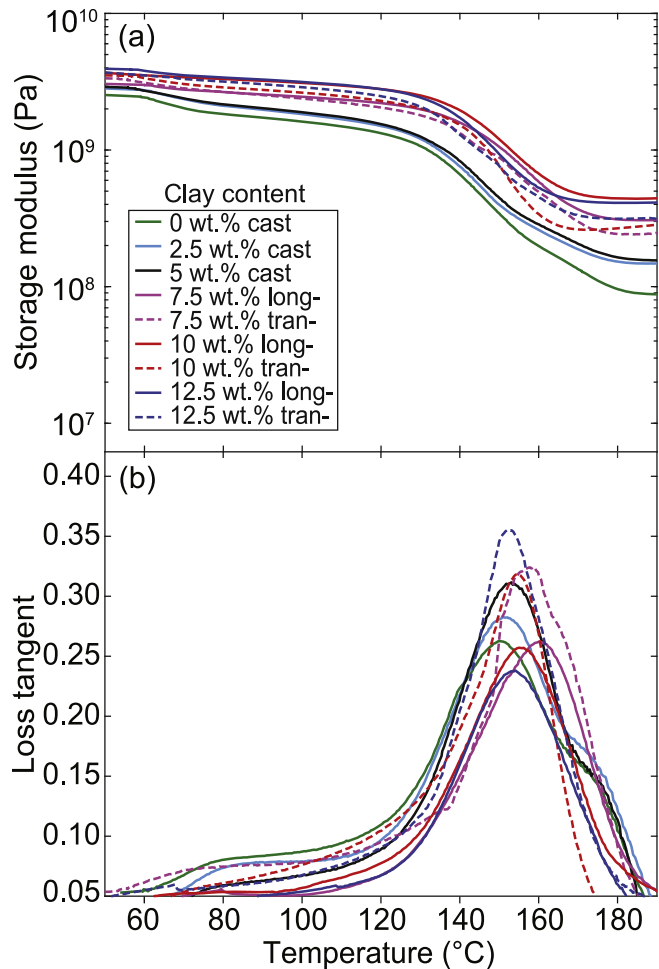


**Fig. 9.** 3-pt. flexure DMA measurements. (a) Representative storage moduli as a function of temperature for all epoxy/clay formulations. (b) The corresponding loss tangent curves.

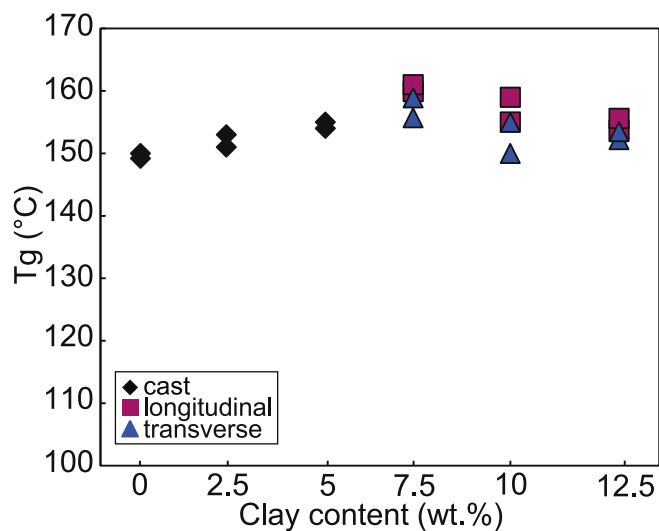


**Fig. 10.** Glass transition temperatures,  $T_g$ , measured from the peak of the loss tangent curves.

bonding in these materials is excellent due to the cross-linking process that occurs after the component has been printed.

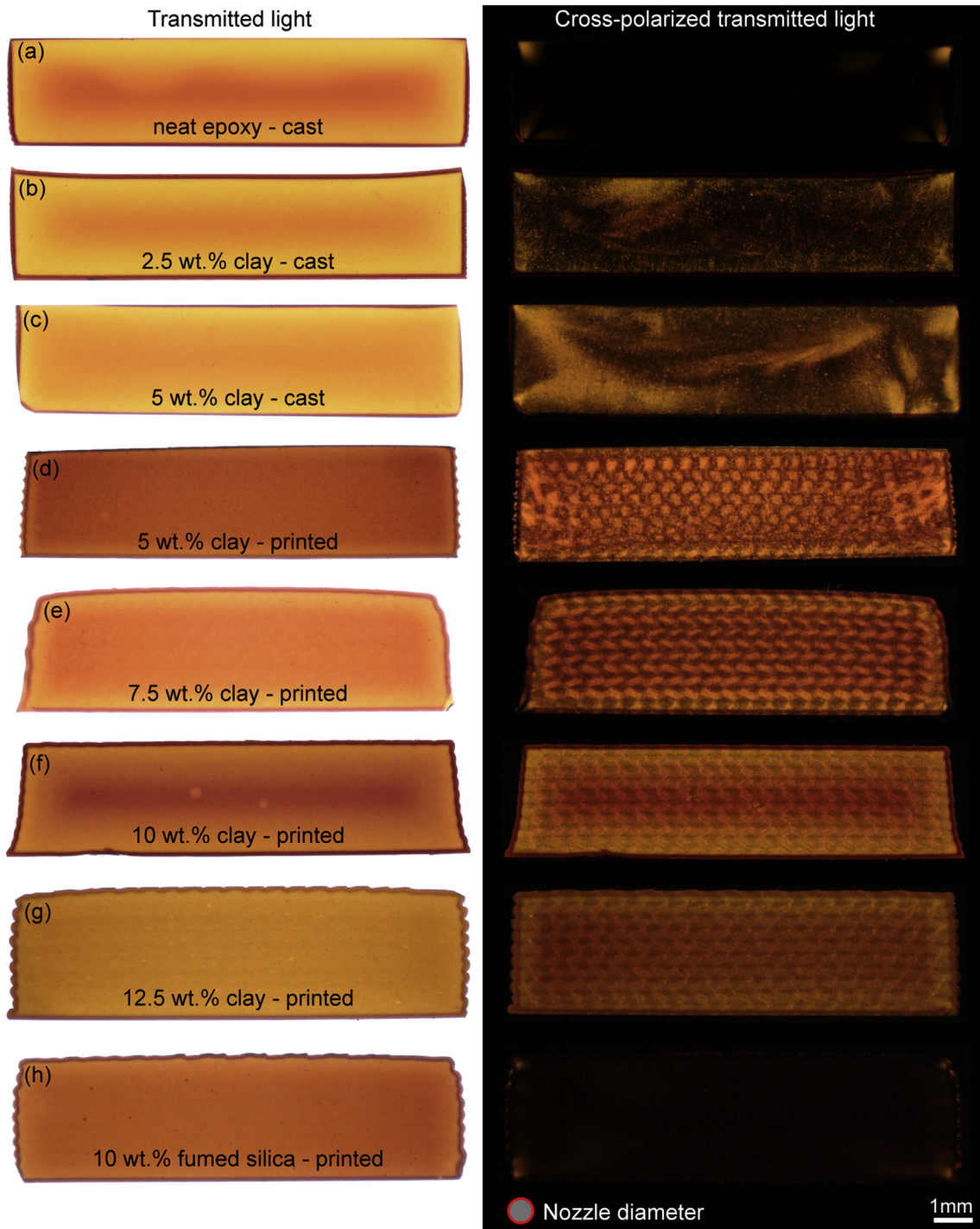


**Fig. 11.** Optical transmitted light micrographs for polished thin slices (<1 mm thick) cut from cast and printed specimens. (a) 0 wt% cast, (b) 2.5 wt% cast, (c) 5 wt% cast, (d) 5 wt% printed, (e) 7.5 wt% printed, (f) 10 wt% printed, (g) 12.5 wt% printed epoxy/nanoclay, and (h) 10 wt% fumed silica, printed. The left-hand column shows normal transmitted light, while the right-hand column shows the same samples observed using crossed polarizers. The patterned birefringence observed in (d)–(g) is indicative of preferred orientation in the nanoclay as a result of the printing process.

Thermal properties in these materials appear to be unaffected by the printing process, so that a wide range of thermal properties should be achievable by utilizing other curing agents that impart different thermal properties.

Cross-polarized light microscopy has proven invaluable in providing straightforward visual characterization of the structure that the printing process imposes on nanocomposite feedstock

materials containing high-aspect ratio particles (e.g. clays). This work has shown that epoxy nanocomposites are promising feedstock materials for direct-write AM, and has highlighted the need for future studies investigating the effects of fiber reinforcement in new high-strength matrices, the possibility of novel nozzle designs to influence and control material directionality, and the effects of carbon-based fillers on the structural and functional properties of

printed composites. These topics are the subject of ongoing research.

## Acknowledgements

This work has been generously supported by the University of Tennessee, the UT Science Alliance through the Joint Directed Research and Development Program (JDRD), and Honeywell Federal Manufacturing & Technology through contract N000230945, administered by Dr. Jamie Messman. The authors would also like to thank Dr. Ryan Kohlmeyer for suggesting polarized light microscopy, Mr. Liam Page and Mr. Robert Pack for assistance preparing flexure test specimens, and Dr. Elizabeth Barker for assistance with rheology measurements. JWK would also like to acknowledge generous support from the UT Chancellor's Fellowship.

## References

- [1] A.A. Azeez, K.Y. Rhee, S.J. Park, D. Hui, *Epoxy clay nanocomposites—processing, properties and applications: a review*, *Compos. B Eng.* 45 (1) (2013) 308–320.
- [2] E.P. Giannelis, Polymer layered silicate nanocomposites, *Adv. Mater.* 8 (1) (1996) 29, <https://doi.org/10.1002/adma.19960080104>.
- [3] S.R. Ha, K.Y. Rhee, S.J. Park, J.H. Lee, Temperature effects on the fracture behavior and tensile properties of silane-treated clay/epoxy nanocomposites, *Compos. B Eng.* 41 (8) (2010) 602–607, <https://doi.org/10.1016/j.compositesb.2010.09.015>.
- [4] T. Lan, T.J. Pinnavaia, Clay-reinforced epoxy nanocomposites, *Chem. Mater.* 6 (12) (1994) 2216–2219.
- [5] A. Zotti, A. Borriello, M. Ricciardi, V. Antonucci, M. Giordano, M. Zarrelli, Effects of sepiolite clay on degradation and fire behaviour of a bisphenol A-based epoxy, *Compos. B Eng.* 73 (2015) 139–148, <https://doi.org/10.1016/j.compositesb.2014.12.019>.
- [6] E. Dunkerley, H. Koerner, R.A. Vaia, D. Schmidt, Structure and dynamic mechanical properties of highly oriented PS/clay nanolaminates over the entire composition range, *Polymer* 52 (4) (2011) 1163–1171.
- [7] G. Galgali, S. Agarwal, A. Lele, Effect of clay orientation on the tensile modulus of polypropylene–nanoclay composites, *Polymer* 45 (17) (2004) 6059–6069.
- [8] M.-I. Chan, K.-t. Lau, T.-t. Wong, M.-p. Ho, D. Hui, Mechanism of reinforcement in a nanoclay/polymer composite, *Compos. B Eng.* 42 (6) (2011) 1708–1712.
- [9] T. Mohan, M. Ramesh Kumar, R. Velmurugan, Rheology and curing characteristics of epoxy–clay nanocomposites, *Polym. Int.* 54 (12) (2005) 1653–1659.
- [10] J.H. Park, S.C. Jana, Mechanism of exfoliation of nanoclay particles in epoxy-clay nanocomposites, *Macromolecules* 36 (8) (2003) 2758–2768, <https://doi.org/10.1021/ma021509c>.
- [11] S. Saber-Samandari, A.A. Khatibi, D. Basic, An experimental study on clay/epoxy nanocomposites produced in a centrifuge, *Compos. B Eng.* 38 (1) (2007) 102–107, <https://doi.org/10.1016/j.compositesb.2006.03.010>.
- [12] B.G. Compton, J.A. Lewis, 3D-Printing of lightweight cellular composites, *Adv. Mater.* 26 (34) (2014) 5930–5935, <https://doi.org/10.1002/adma.201401804>.
- [13] X. Wang, M. Jiang, Z. Zhou, J. Gou, D. Hui, 3D printing of polymer matrix composites: a review and prospective, *Compos. B Eng.* 110 (Supplement C) (2017) 442–458. <https://doi.org/10.1016/j.compositesb.2016.11.034>.
- [14] R.D. Farahani, M. Dubé, D. Therriault, Three-dimensional printing of multifunctional nanocomposites: manufacturing techniques and applications, *Adv. Mater.* 28 (28) (2016) 5794–5821.
- [15] T. Hofstätter, D.B. Pedersen, G. Tosello, H.N. Hansen, State-of-the-art of fiber-reinforced polymers in additive manufacturing technologies, *J. Reinforc. Plast. Compos.* 36 (15) (2017) 1061–1073.
- [16] P. Parandush, D. Lin, A review on additive manufacturing of polymer-fiber composites, *Compos. Struct.* 182 (2017) 36–53.
- [17] R.R. Collino, T.R. Ray, R.C. Fleming, J.D. Cornell, B.G. Compton, M.R. Begley, Deposition of ordered two-phase materials using microfluidic print nozzles with acoustic focusing, *Extreme Mechanics Letters* 8 (2016) 96–106. <https://doi.org/10.1016/j.eml.2016.04.003>.
- [18] B.G. Compton, N.S. Hmeidat, R.C. Pack, M. Heres, J.R. Sangoro, Electrical and mechanical properties of 3D-printed graphene-reinforced epoxy, *JOM (J. Occup. Med.)* 70 (3) (2018) 292–297.
- [19] B.G. Compton, J.W. Kemp, T.V. Novikov, R.C. Pack, C.I. Nlebedim, C.E. Duty, O. Rios, M.P. Paranthaman, Direct-write 3D printing of NdFeB bonded magnets, *Mater. Manuf. Process.* 33 (1) (2018) 109–113, <https://doi.org/10.1080/10426914.2016.1221097>.
- [20] L. Friedrich, R. Collino, T. Ray, M. Begley, Acoustic control of microstructures during direct ink writing of two-phase materials, *Sensor Actuator Phys.* 268 (2017) 213–221. <https://doi.org/10.1016/j.sna.2017.06.016>.
- [21] J.P. Lewicki, J.N. Rodriguez, C. Zhu, M.A. Worsley, A.S. Wu, Y. Kanarska, J.D. Horn, E.B. Duoss, J.M. Ortega, W. Elmer, 3D-Printing of meso-structurally ordered carbon fiber/polymer composites with unprecedented orthotropic physical properties, *Sci. Rep.* 7 (2017) 43401.
- [22] S. Malek, J.R. Raney, J.A. Lewis, L.J. Gibson, Lightweight 3D cellular composites inspired by balsa, *Bioinspiration Biomimetics* 12 (2) (2017) 026014.
- [23] J.R. Raney, B.G. Compton, J. Mueller, T.J. Ober, K. Shea, J.A. Lewis, Rotational 3D printing of damage-tolerant composites with programmable mechanics, *Proc. Natl. Acad. Sci. Unit. States Am.* 115 (6) (2018) 1198–1203, <https://doi.org/10.1073/pnas.1715157115>.
- [24] P. Calvert, T.L. Lin, H. Martin, Extrusion freeform fabrication of chopped-fibre reinforced composites, *High Perform. Polym.* 9 (4) (1997) 449–456.
- [25] J. Peng, T.L. Lin, P. Calvert, Orientation effects in freeformed short-fiber composites, *Compos. Appl. Sci. Manuf.* 30 (2) (1999) 133–138. [https://doi.org/10.1016/S1359-835X\(98\)00110-9](https://doi.org/10.1016/S1359-835X(98)00110-9).
- [26] J.A. Lewis, Direct ink writing of 3D functional materials, *Adv. Funct. Mater.* 16 (17) (2006) 2193–2204, <https://doi.org/10.1002/adfm.200600434>.
- [27] D. Therriault, S.R. White, J.A. Lewis, Rheological behavior of fugitive organic inks for direct-write assembly, *Appl. Rheol.* 17 (1) (2007) 10112–11411.
- [28] B.G. Compton, B.K. Post, C.E. Duty, L. Love, V. Kunc, Thermal analysis of additive manufacturing of large-scale thermoplastic polymer composites, *Addit. Manuf.* 17 (2017) 77–86. <https://doi.org/10.1016/j.addma.2017.07.006>.
- [29] R.B. Dinwiddie, L.J. Love, J.C. Rowe, Real-time process monitoring and temperature mapping of a 3D polymer printing process, SPIE defense, security, and sensing, International Society for Optics and Photonics (2013) 87050L.
- [30] L.J. Love, V. Kunc, O. Rios, C.E. Duty, A.M. Elliott, B.K. Post, R.J. Smith, C.A. Blue, The importance of carbon fiber to polymer additive manufacturing, *J. Mater. Res.* 29 (17) (2014) 1893–1898, <https://doi.org/10.1557/jmr.2014.212>.
- [31] T.-M. Wang, J.-T. Xi, Y. Jin, A model research for prototype warp deformation in the FDM process, *Int. J. Adv. Manuf. Technol.* 33 (11–12) (2007) 1087–1096, <https://doi.org/10.1007/s00170-006-0556-9>.
- [32] X. Fernández-Francos, S.G. Kazarian, X. Ramis, Á. Serra, Simultaneous monitoring of curing shrinkage and degree of cure of thermosets by attenuated total reflection Fourier transform infrared (ATR FT-IR) spectroscopy, *Appl. Spectrosc.* 67 (12) (2013) 1427–1436.
- [33] O. Rios, W. Carter, B.K. Post, P. Lloyd, D. Fenn, C. Kutchko, R. Rock, K. Olson, B.G. Compton, 3D printing via ambient reactive extrusion, *Materials Today Communications* (2018) (In press).
- [34] S.H. Ahn, M. Montero, D. Odell, S. Roundy, P.K. Wright, Anisotropic material properties of fused deposition modeling ABS, *Rapid Prototyp. J.* 8 (4) (2002) 248–257, <https://doi.org/10.1108/13552540210441166>.
- [35] C.E. Duty, V. Kunc, B. Compton, B. Post, D. Erdman, R. Smith, R. Lind, P. Lloyd, L. Love, Structure and mechanical behavior of big area additive manufacturing (BAAM) materials, *Rapid Prototyp. J.* 23 (1) (2017).
- [36] V. Kishore, C. Ajinjeru, A. Nycz, B. Post, J. Lindahl, V. Kunc, C. Duty, Infrared preheating to improve interlayer strength of big area additive manufacturing (BAAM) components, *Additive Manufacturing* 14 (2017) 7–12.
- [37] Y.R. Ham, S.H. Kim, Y.J. Shin, D.H. Lee, M. Yang, J.H. Min, J.S. Shin, A comparison of some imidazoles in the curing of epoxy resin, *J. Ind. Eng. Chem.* 16 (4) (2010) 556–559.
- [38] SpecialChem, Garamite 7305, Available from: <https://cosmetics.specialchem.com/product/i-byk-altana-group-garamite-7305>.
- [39] BYK, Garamite 7305, Available from: <http://www.byk.com/en/additives/additives-by-name/garamite-7305.php>.
- [40] M. Alexandre, P. Dubois, Polymer-layered silicate nanocomposites: preparation, properties and uses of a new class of materials, *Mater. Sci. Eng. R Rep.* 28 (1–2) (2000) 1–63.
- [41] A. Nohales, L. Solar, I. Porcar, C.I. Vallo, C.M. Gomez, Morphology, flexural, and thermal properties of sepiolite modified epoxy resins with different curing agents, *Eur. Polym. J.* 42 (11) (2006) 3093–3101.
- [42] Compton, B.G. and J.A. Lewis, 3D-Printed Polishing Pad for Chemical-Mechanical Planarization (CMP). U.S. Provisional Patent Application No. 61988555.
- [43] Standard Test Methods for Flexural Properties of Unreinforced and Reinforced Plastics and Electrical Insulating Materials.
- [44] M. Dinkgreve, J. Paredes, M.M. Denn, D. Bonn, On different ways of measuring “the” yield stress, *J. Non-Newtonian Fluid Mech.* 238 (Supplement C) (2016) 233–241. <https://doi.org/10.1016/j.jnnfm.2016.11.001>.
- [45] A. Gu, G. Liang, Thermal degradation behaviour and kinetic analysis of epoxy/montmorillonite nanocomposites, *Polym. Degrad. Stabil.* 80 (2) (2003) 383–391.
- [46] N. Rose, M. Le Bras, S. Bourbigot, R. Delobel, Thermal oxidative degradation of epoxy resins: evaluation of their heat resistance using invariant kinetic parameters, *Polym. Degrad. Stabil.* 45 (3) (1994) 387–397.
- [47] G. Camino, G. Tartaglione, A. Frache, C. Manferti, G. Costa, Thermal and combustion behaviour of layered silicate–epoxy nanocomposites, *Polym. Degrad. Stabil.* 90 (2) (2005) 354–362.